Journal of Electronic Materials
https://doi.org/10.1007/s11664-024-11376-3

ORIGINAL RESEARCH ARTICLE

Effects of Various Substrates on the Structure and Properties of $BiFe_{0.91}Zr_{0.09}O_3$ Thin Films

Zhen Jiang[1] · Zhibiao Ma[1] · Yuan Liu[1] · Jingxian He[1] · Shuhui Sun[1] · Zhenfeng Jing[1] · Fengqing Zhang[1]

Received: 6 April 2024 / Accepted: 7 August 2024

Abstract

$BiFe_{0.91}Zr_{0.09}O_3$ (9BFZrO)/$LaNiO_3$ (LNO)/MgO and 9BFZrO/LNO/Si multilayers were prepared by the sol–gel method using MgO and Si single crystals as substrates, and LNO films with a thickness of approximately 50 nm were deposited by magnetron sputtering to form bottom electrodes and transition layers. The effects of different substrates on the crystal structure, phase composition, oxygen vacancy content, ferroelectric properties, dielectric properties, leakage mechanism, and ageing properties of the 9BFZrO films were systematically analysed. X-ray diffraction showed that the prepared 9BFZrO thin films had a structure composed of both rhombic *R*3*c* and orthogonal *Pnma* phases, and the films prepared on the MgO substrate contained a significant amount of the *R*3*c* phase. SEM analysis showed that the thin film prepared on the MgO substrate had a relatively large grain size. X-ray photoelectron spectroscopy showed that the Fe^{2+} content and oxygen vacancy defect concentration of the MgO substrate samples were relatively low. The thin film prepared on the MgO substrate has a high residual polarization strength ($2P_r = 60.28$ μC/cm^2) and a low leakage current density (4.71×10^{-6} A/cm^2). After 90 days of room-temperature ageing, the residual polarization strength ($2P_r$) of the film on the MgO substrate decreased by 16.8%, with a lower ageing degree and better stability.

Keywords Substrate · ferroelectric performance · lattice mismatch · ageing properties

Introduction

A multiferroic material refers to a material with two or more ordered parameters, such as ferroelectricity, ferromagnetism (antiferromagnetism), and ferroelasticity, and a series of rich physical properties due to the interaction between ordered parameters.[1,2] $BiFeO_3$ (BFO) is a scarce material that exhibits multiferroic properties at ambient temperature and has become a research hotspot due to its excellent ferroelectric properties, ability to perform magnetoelectric coupling, and photovoltaic effects.[3,4] Because of its ferroelectricity and G-type antiferromagnetism at ambient temperature, BFO possesses elevated Curie temperature ($T_C = 1103$ K) and Neil temperature ($T_N = 647$ K) values. Therefore, BFO has become a popular topic for in-depth investigations of multiferroic materials, garnering universal interest from materials scholars.[5–7] However, Fe^{3+} in pure-phase BFO tends to transform into Fe^{2+} and generate oxygen vacancies, leading to increased leakage current and other issues.[8] Therefore, by doping of components, creating solid solutions, creating double- or multilayer composite films, and changing substrates, researchers can create high-quality films.[9–13] Substrates are essential for the development of thin films and for testing certain characteristics. Different substrates exhibit different lattice constants, and a lattice mismatch occurs in the upper layer. The choice and orientation of the substrate directly impact the crystal structure and other characteristics of the thin film.[14] Therefore, understanding how various substrates affect the composition and characteristics of thin films is essential.

Ujimoto et al.[15] examined the composition and ferroelectric characteristics of epitaxial thin films of BFO with various lattice mismatches and found that lattice mismatches led to the generation of defects in grains and affected polarization reversal. In thin films with low mismatch strengths, the grain density decreases with increasing leakage current and coercive field. Park et al.[16] prepared BFO thin films on indium tin oxide (ITO) and Pt utilizing pulsed laser deposition to apply substrates and found that the leakage current

✉ Fengqing Zhang
zhangfengqing615@163.com

[1] School of Materials Science and Engineering, Shandong Jianzhu University, Jinan 250101, Shandong, China

Published online: 22 August 2024

of the Pt substrate was 8×10^{-2} A/cm^2, the ITO substrate leakage current was 7×10^{-5} A/cm^2, and the leakage current density on the ITO substrate decreased. Hou et al.[17] prepared $BaTiO_3$/$BiFeO_3$ (BTO/BFO) bilayer films and found that introducing BTO films generated stress that prevented the formation of M_C-phase BFO and greatly contributed to the reduction in dielectric loss and leakage current in BFO films; as a result, the ferroelectric and piezoelectric properties of the films were improved. Wang et al.[18] prepared thin coatings on stainless steel substrates buffered with $LaNiO_3$ (LNO), and after a buffer layer was incorporated, the dielectric loss and density of leakage current decreased substantially. Therefore, investigating the impacts of various substrates on the structure and properties of BFO thin films is a viable endeavour.

Based on the above literature, replacing substrates with different lattice constants can generate substrate stress on thin films, which can significantly affect the characteristics and structure of BFO thin films. However, the literature contains many discussions regarding the impacts of various substrates on the ferroelectricity, ageing, and crystal structure alterations of thin films. In preliminary experiments, we improved the performance of BFO thin films using ion doping and found that 9BFZrO thin films achieved improved performance over pure BFO thin films.[19] In this paper, the mechanism by which substrates impact the ferroelectricity and phase transition of 9BFZrO thin films was comprehensively analysed. Specifically, magnesium oxide (MgO) and silicon (Si) single-crystal wafers with the same orientation (<110>) were applied as substrates to study the impact of various substrates on the composition and electrical characteristics of 9BFZrO thin-film samples.

Experimental Procedure

MgO and Si single-crystal wafers were selected as substrates, and magnetron sputtering was used to prepare approximately 50-nm-thick LNO thin films as bottom electrodes. The sol–gel method was used, with $Fe(NO_3)_3{\cdot}9H_2O$, $Bi(NO_3)_3{\cdot}5H_2O$, and $Zr(NO_3)_4{\cdot}5H_2O$ used as solutes. Since bismuth salt is volatile at high temperatures, $Bi(NO_3)_3{\cdot}5H_2O$ was weighed in excess of 5%. A 1:3 ratio of CH_3CH_2OH to CH_3COOH was used as the solvent, and $CH_3COCH_2COCH_3$ was added as the chelating agent. The mixture was stirred at a constant speed for 12 h to generate a uniform and stable semitransparent dark red solution. The LNO/MgO and LNO/Si substrates were placed on a homogenizer for rotary coating, dried on a heating plate, and placed in a rapid annealing furnace for pyrolysis. The final heat treatment was performed at 525°C to fully crystallize the thin film. The above steps were repeated until the thin-film sample reached the expected thickness, and 9BFZrO/LNO/MgO and 9BFZrO/LNO/Si multilayer thin films were constructed.

In this experiment, a Bruker D8 Advance x-ray diffractometer was used to analyse the crystal structure of the 9BFZrO thin films. The lattice phase transitions of the thin films were characterized using a LabRAM HR 800 Raman spectrometer. The surface morphology and grain size of the thin films were characterized using a Hitachi SU8010 scanning electron microscope. The changes in the valence states of the elements in the thin film were determined using a ESCALAB 250xi XPS analyser. A Radiant Technologies ferroelectric tester was used to test the ferroelectric and leakage characteristics of the thin films. The dielectric constant and dielectric loss were calculated using a TH2828S dielectric tester.

Results and Discussion

Figure 1a shows the x-ray diffraction (XRD) patterns of the 9BFZrO thin films on MgO and Si substrates, and the prepared samples are all polycrystalline in structure; Fig. 1b shows the magnified (001) and (002) diffraction peaks of the 9BFZrO film. The positions of the dashed lines indicate the corresponding diffraction peaks of the single-crystal bulk BFO. Compared with the MgO thin-film samples, the Si thin-film samples no longer exhibit clear peak separation but merge to form a single peak. This change resulted from a lattice mismatch caused by different lattice constants between the thin film and substrate, resulting in differences in the crystal structure of the thin film. The lattice mismatch degree is calculated by Eq. 1 as follows:

$$S = \frac{\alpha_s - \alpha_f}{\alpha_s}, \tag{1}$$

where α_s is the substrate lattice constant, and α_f is the lattice constant of the thin film. The lattice constant of the MgO substrate is 4.216 Å, and the lattice constant of the Si substrate is 5.431 Å. The lattice mismatches with the 9BFZrO thin film are 5.9% and 26.9%, respectively. Compared to those of bulk BFO, the (001) and (002) diffraction peaks of the 9BFZrO thin films on MgO and Si substrates shift towards higher angles, corresponding to a decrease in the lattice constant. Moreover, the degree of shift in thin films prepared on Si substrates is greater than that on MgO substrates, which can be explained by in-plane stress. Low-angle movement corresponds to lattice elongation caused by compressive stress, while high-angle movement reflects lattice compression caused by tensile stress.[20] The lattice constants of MgO (4.216 Å) and Si (5.431 Å) are greater than that of BFO (3.965 Å), indicating that the 9BFZrO thin films exhibit tensile strain on the MgO and Si substrates. To

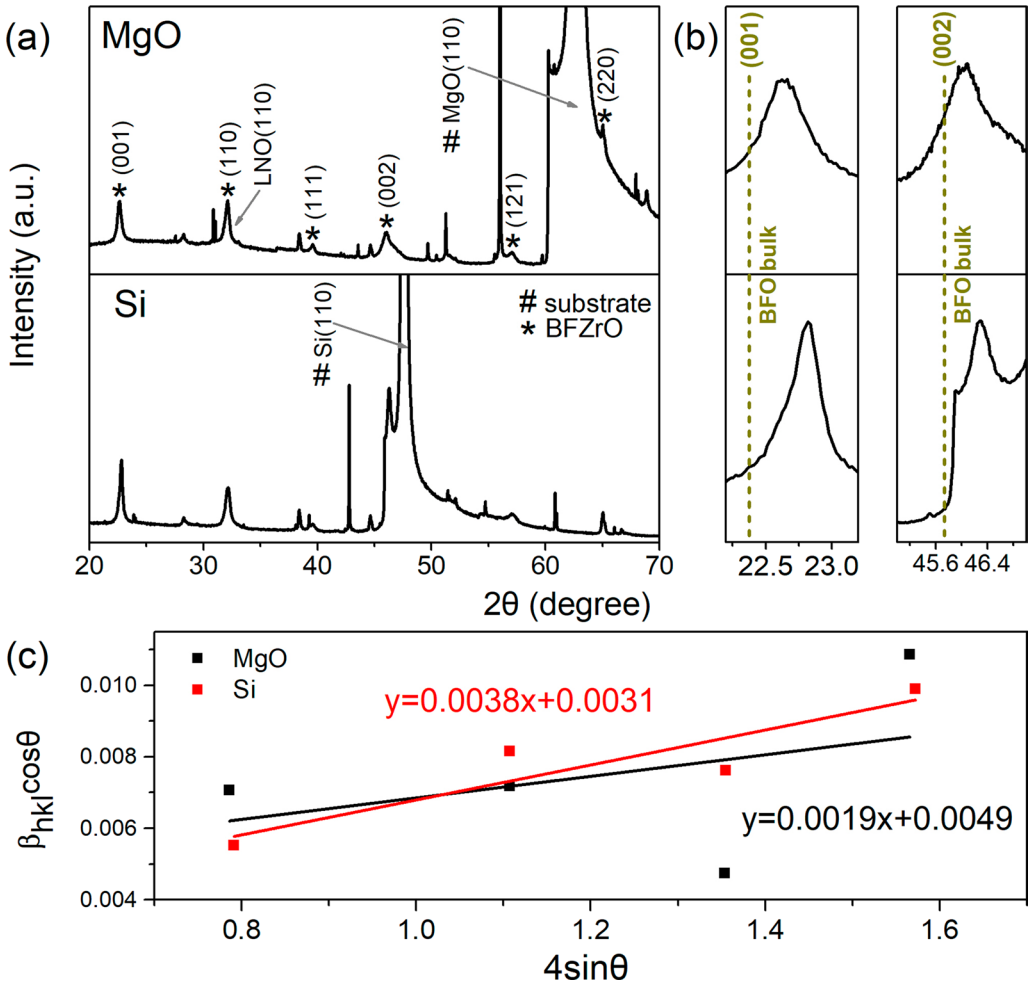

Fig. 1 (a) XRD pattern of 9BFZrO thin films on MgO and Si substrates, (b) magnified (001) and (002) diffraction peaks, and (c) Williamson–Hall plot.

verify our hypothesis, we further determined the strain of the thin-film sample using the Williamson–Hall formula,[21] which is expressed as follows:

$$\beta_{hkl}\cos\theta = \frac{K\lambda}{D} + 4\tau\sin\theta, \tag{2}$$

where β_{hkl} is the half-maximum width in radians, which is the full width at half maximum (FWHM), D is the grain size, K is a constant equal to 0.89, λ is the x-ray wavelength, θ is the Bragg diffraction angle, and τ is the lattice strain. $\beta_{hkl}\cos\theta$ was separated, and the y-axis and x-axis of the $4\sin\theta$ function graphs were drawn based on the obtained intercept and slope values to analyse the lattice strain of the sample, where y is $\beta_{hkl}\cos\theta$ and x is $4\sin\theta$. Figure 1c shows the Williamson–Hall plot of the 9BFZrO thin films on MgO and Si substrates. The fitted straight-line slopes (0.0038 and 0.0019) of both samples were positive, confirming the existence of tensile strain.[22] The larger slope of the Si substrate sample indicates that it has generated greater tensile stress.

To investigate the impact of substrate stress on the crystal structure of the 9BFZrO thin films, we performed Raman spectroscopy. A group theory study revealed that the BFO crystal in the $R3c$ phase exhibited 13 Raman-active modes[23,24]: $\Gamma_{\mathrm{Raman},R3c} = 4A_1 + 9E$, where $LaAlO_3$ and $LaMnO_3$ are very similar to rhombic $R3c$ perovskite.[25] Figure 2a shows the Raman spectra of the 9BFZrO thin films on the MgO and Si substrates in the range of 50–650 nm. The Raman spectroscopy data obtained by direct measurement were further fitted, as shown in Fig. 2b and c. Table 1 shows the corresponding positions of each Raman mode, which is consistent with the research results of Fukumura[26] and Abdel et al.[27] The Raman modes with frequencies below 170 cm^{-1} correspond to the vibrations of Bi atoms, while the Raman modes with frequencies between 170 cm^{-1} and

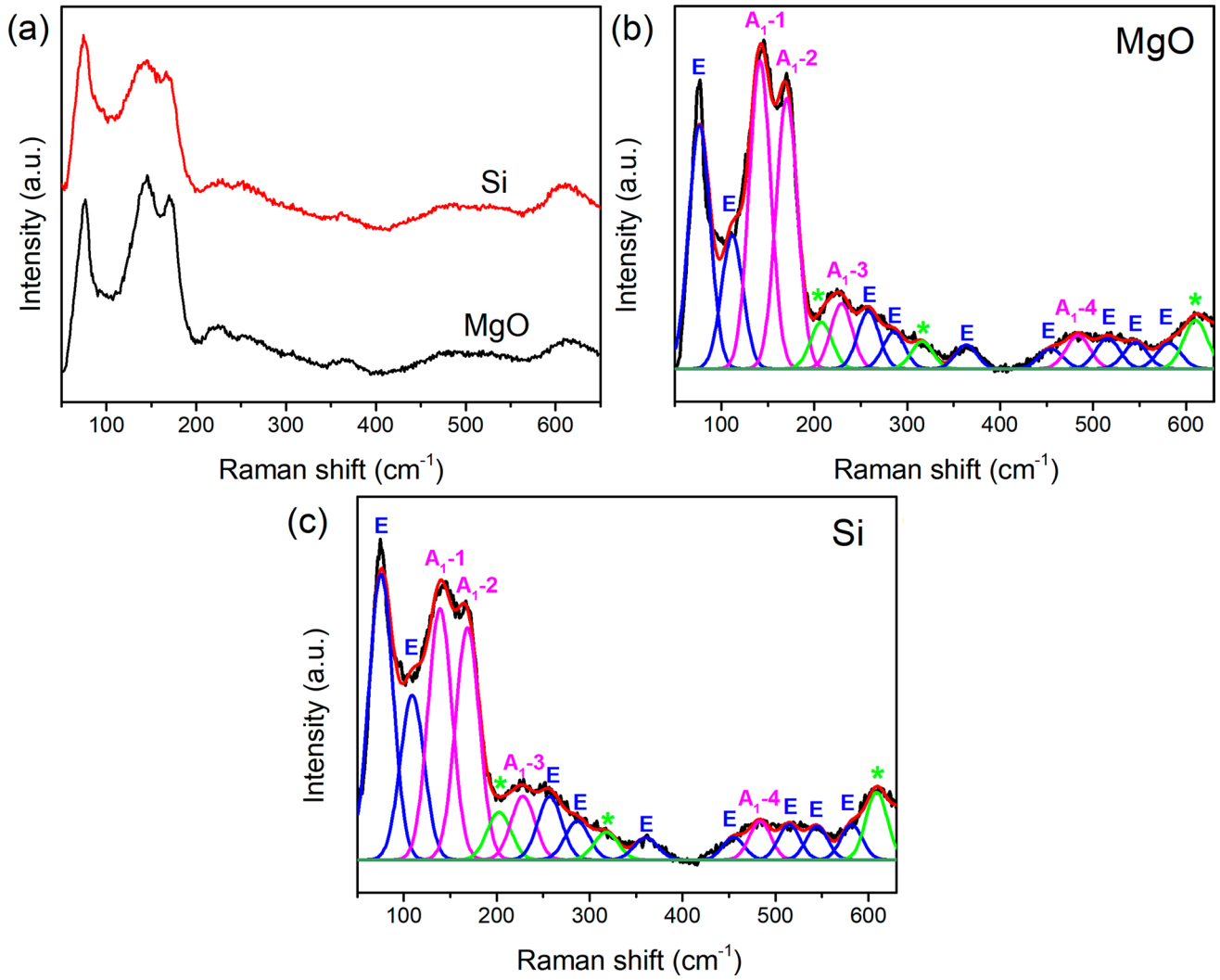

Fig. 2 (a) Raman spectra of 9BFZrO thin films on MgO and Si substrates; (b, c) Raman spectra fitting.

260 cm^{-1} correspond to the vibrations of Fe atoms. The Raman modes with frequencies greater than 260 cm^{-1} are mostly associated with the motion of oxygen.[29] Furthermore, all 9BFZrO films have distinct peaks at approximately 200 cm^{-1}, 320 cm^{-1}, and 610 cm^{-1} (shown by asterisks in Fig. 2b and c), which correspond to the orthorhombic *Pnma* phase of BFO films.[28,29] These peaks are consistent with the results reported by Iliev et al. for $LaMnO_3$ and $YMnO_3$ with orthorhombic *Pnma* space groups.[30] Therefore, the 9BFZrO thin-film samples on the MgO and Si substrates coexist in the rhombic *R*3*c* and orthogonal *Pnma* phases, which is consistent with our previous research results.[19] In addition, it can be seen from the figure that the relative intensity of the A_1-1 Raman mode in the thin-film sample prepared on the MgO substrate is significantly enhanced, indicating that the sample has greater diamond distortion and greater *R*3*c* phase content. The *Pnma* Raman mode of the Si substrate sample near 610 cm^{-1} has a lower displacement and higher relative intensity, indicating that the sample contains more of the *Pnma* phase. This can be explained by tensile strain, as studies have shown that when tensile stress is continuously applied, the BFO lattice transitions from the rhombic R-phase to the orthogonal phase.[31] Compared to that of the MgO substrate, the excessive tensile stress generated by the Si substrate causes the sample to contain more orthogonal phases, which may affect its electrical properties.

Figure 3a and b show the SEM surface morphology of the thin 9BFZrO layers on the MgO and Si substrates. The grain development of all the samples was significantly compact. The average grain sizes of the two samples are approximately 57.6 nm and 52.5 nm, respectively, indicating that the MgO substrate sample has a relatively large grain size, which is consistent with the XRD analysis results. Figure 3c and d show SEM cross-sectional images of the 9BFZrO thin films on the MgO and Si substrates. Clear interfaces of 9BFZrO/LNO, LNO/MgO, and LNO/

Table 1 Raman modes of the 9BFZrO thin films

Raman mode	MgO (cm^{-1})	Si (cm^{-1})
E	76.48	75.05
E	111.67	109.07
A_1-1	141.53	138.93
A_1-2	170.35	168.43
Pnma	207.55	202.51
A_1-3	229.27	228.22
E	258.21	257.12
E	285.74	286.69
Pnma	315.96	317.89
E	363.42	360.64
E	454.57	454.93
A_1-4	483.87	483.38
E	515.81	514.68
E	545.86	544.72
E	581.72	581.85
Pnma	610.33	608.78
R^2 fitting	0.9947	0.9988

Both A_1 and *E* Raman modes correspond to the *R*3*c* space group.

Si can be observed in the images, with thicknesses of approximately 800 nm and 50 nm for the 9BFZrO and LNO layers, respectively.

XPS can further reveal the valence state changes and defect states of various elements in the 9BFZrO thin films. In general, the extent to which the film current leaks is directly impacted by the valence variation in Fe^{3+} and the number of oxygen vacancies in the 9BFZrO thin films, thus influencing its overall performance. Figure 4a and b show the Fe $2p_{3/2}$ fitting of 9BFZrO thin films on various substrates. The fitting results indicate that the Fe $2p_{3/2}$ peaks of both samples are composed of Fe^{2+} and Fe^{3+} and are near 709.5 eV and 711 eV, respectively.[32,33] The defect equation states that the concentration of Fe^{2+} is exactly proportional to the concentration of oxygen vacancies as follows[34]:

$$2Fe_{Fe}^{X} + O_{O}^{X} \rightarrow 2Fe_{Fe}^{'} + V_{\ddot{O}} + \frac{1}{2}O_2 \uparrow \quad (3)$$

The figure shows that the ratio of the fitting areas of Fe^{3+} and Fe^{2+} in the samples of the MgO and Si substrates is 2.50 and 2.23, respectively. The results indicate that the Fe^{2+} content in the film with the MgO substrate is lower. Figure 4c and d show high-resolution XPS spectra of O 1*s* orbitals in thin film samples on the MgO and Si substrates. The O 1*s* peak was fit using a Gaussian Lorentz curve. The peak at binding energy of approximately 529 eV is attributed to lattice oxygen (O_L), while the peak at approximately 531 eV encompasses oxygen vacancies (O_V) and adsorbed oxygen (O_C).[35] The ratios of the fitting areas for O_V and O_L are 0.49 and 0.52, respectively. The thin film using MgO as the substrate exhibits a comparatively low concentration of oxygen vacancy defects, which aligns with the fitting results obtained for Fe $2p_{3/2}$ orbitals.

Figure 5a shows the leakage current density curve (*J*–*E* curve) of the 9BFZrO thin films on the MgO and Si substrates. The study revealed that the *J*–*E* curve displays asymmetry in positive and negative electric fields. This asymmetry results from the disparate stress levels induced by the two substrates and the distinct built-in potentials created by the top and bottom electrodes. The leakage current densities of the samples fabricated on the MgO and Si substrates under a positive electric field of 200 kV/cm were approximately 4.71×10^{-6} A/cm^2 and 7.16×10^{-6} A/cm^2, respectively. The *J* value of the sample prepared on the MgO substrate was slightly lower than that of the Si substrate sample. This may result from the combined effects of a smaller lattice mismatch, lower oxygen vacancy and Fe^{2+} defect concentrations, and larger average grain size in the MgO substrate samples.[36] α is the slope of the log(*J*)–log(*E*) curve, and through α, the conductivity mechanism of the thin film is derived, as shown in Fig. 5b. The leakage current mechanism is shown in Table 2.

In Table 2, *q* represents the charge of an electron, μ represents the mobility of the carrier, Ne represents the concentration of the carrier, ε_r represents the relative dielectric constant, ε_0 represents the vacuum dielectric constant, *d* is the thickness of the film, *K* is the optical dielectric constant, *A*, *B*, *C*, and *D* are constants, *E* is the electric field strength, φ_b is the Schottky barrier height, E_t is the trap ionization energy, K_b is the Boltzmann constant, and *T* is the thermodynamic temperature. From the above leakage mechanism, it can be inferred that the log(*J*)–log(*E*) linear slopes of the ohmic conduction and SCLC mechanisms are 1 and 2, respectively. The fitting slopes of the two samples in Fig. 5b (α) are close to 1, indicating that the leakage current mechanism of the 9BFZrO thin films on the MgO and Si substrates is mainly an ohmic conduction mechanism.

Figure 6 shows the hysteresis loop (P–E) diagram of the 9BFZrO thin films on the MgO and Si substrates, with a test electric field of 990 kV/cm and a test frequency of 1 kHz. The two thin-film samples show residual polarization strength ($2P_r$) of approximately 60.28 μC/cm^2 and 25.17 μC/cm^2, respectively, and the residual polarization intensity of the Si substrate sample is relatively low. Research has shown that when tensile stress is continuously applied, the BFO lattice transitions from the rhombic R-phase to the low-symmetry M_B phase and then to the orthorhombic phase, which is a non-ferroelectric phase with opposite polarity.[40–42] XRD analysis revealed that, compared with the MgO substrate, the Si substrate provided greater tensile stress to the 9BFZrO film. Therefore, the decrease in residual polarization of the Si substrate sample may result from the presence of more orthogonal phases in the film, leading to a decrease in the

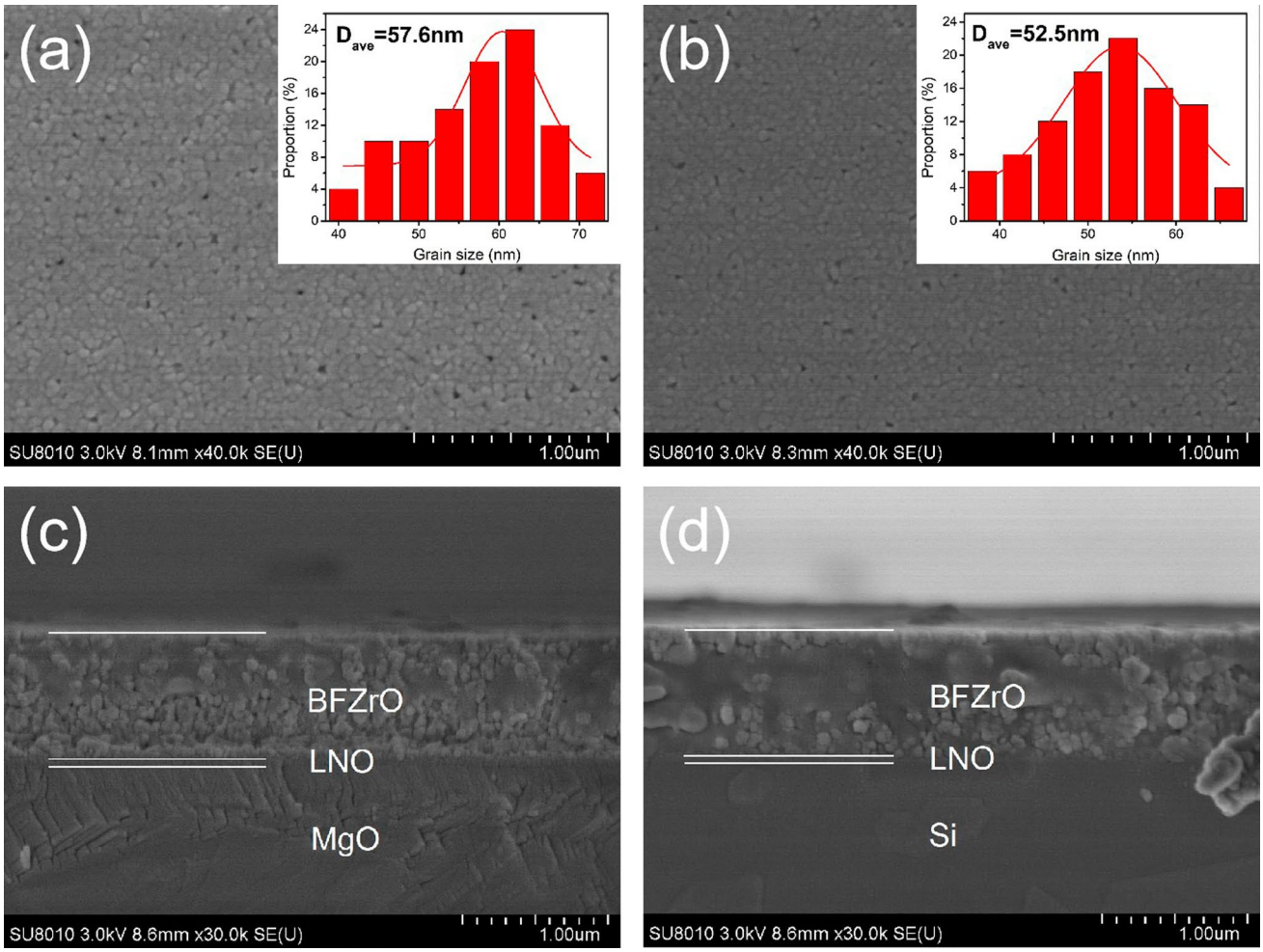

Fig. 3 (a, b) SEM surface morphology of 9BFZrO thin films on MgO and Si substrates; (c, d) SEM cross-sectional view.

ferroelectric properties of the film, which is consistent with Raman analysis. Furthermore, the ferroelectric characteristics of thin films are influenced by the concentration of defects and the grain size. The Si substrate sample exhibits a significant abundance of oxygen vacancies and Fe^{2+} defects, resulting in high leakage current density and small average grain size; as a result, it is difficult to flip ferroelectric domains, and the residual polarization strength of the thin-film sample is reduced.

Figure 7 shows the relative dielectric constants of the 9BFZrO thin-film samples on the MgO and Si substrates (ε_r) and the dielectric loss (tanδ) as a function of the testing frequency. The dielectric constant decreases with increasing frequency, which is related to the polarization mechanism.[43–45] In the low-frequency range, the electrons accumulate at the grain boundaries and thus produce polarization if they move to the grain boundaries as a result of thermal motion or field stress. However, with the increase of the measuring frequency, the pile-up effect is reduced because the electrons continuously reverse their direction of motion, and hence the polarization is decreased.[45] When the frequency is greater than 10^5 Hz, the dielectric loss of both samples is significantly increased, possibly because the flipping of ferroelectric domains cannot match the flipping of the electric field.[46] The graph shows that the MgO substrate sample has a relatively large dielectric constant and low dielectric loss, indicating good dielectric performance. This property may result from a combination of a smaller lattice mismatch, lower defect concentration, and larger grain size in the sample.

After the application of ferroelectric thin films, the reliability of a device is almost completely dependent on the stability of the ferroelectric thin films, so the anti-ageing performance of thin films is particularly important. After the films were aged for 90 days at room temperature, the hysteresis loops of the 9BFZrO films on various substrates were re-evaluated. The results are shown in Fig. 8a and b. The residual polarization intensity ($2P_r$) of the thin films decreased by 16.8% and 45.6% on the MgO and Si substrates, respectively. The thin film produced on the MgO

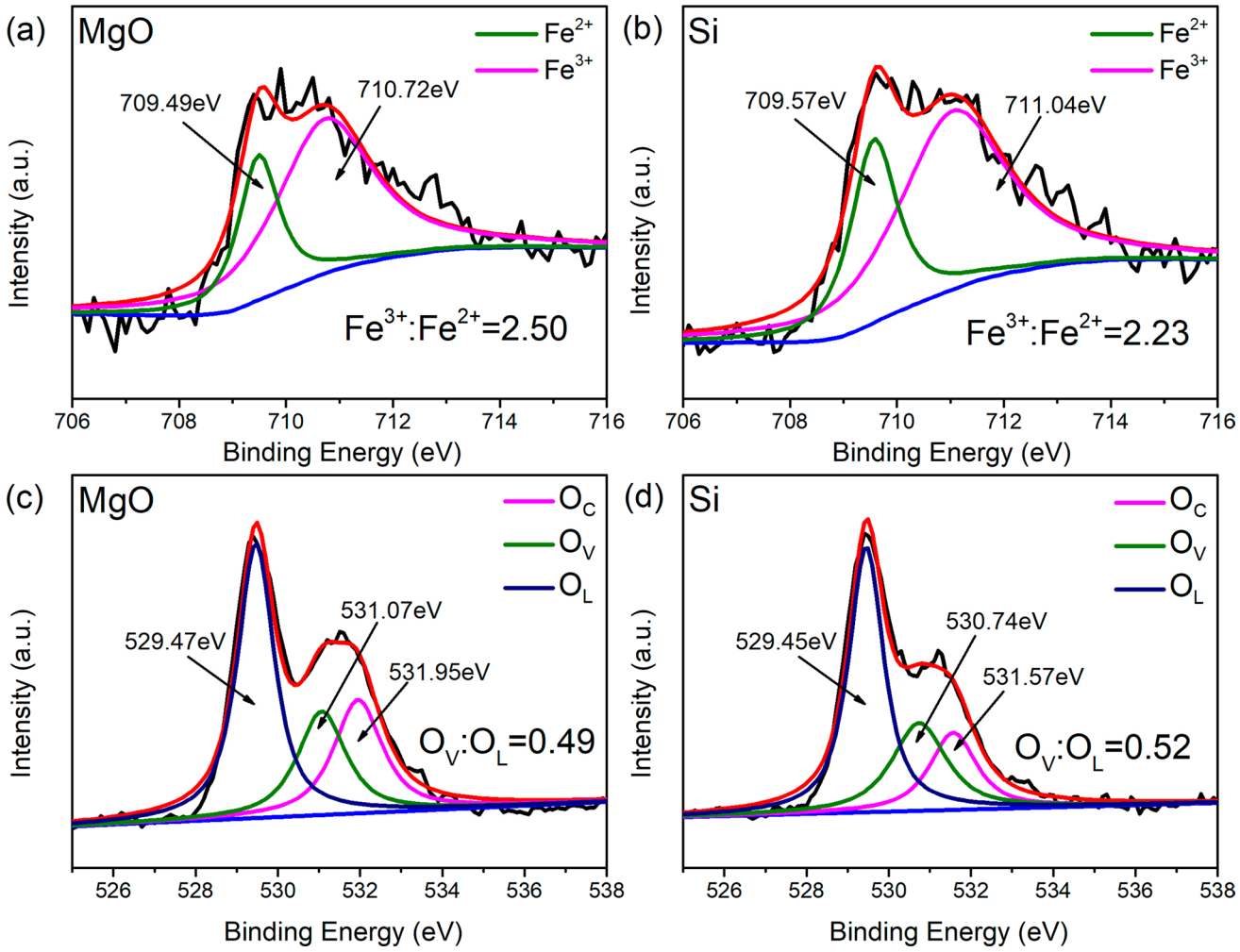

Fig. 4 (a, b) Fe $2p_{3/2}$ orbital XPS fitting diagram; (c, d) O 1*s* orbital XPS fitting diagram of 9BFZrO thin films on MgO and Si substrates.

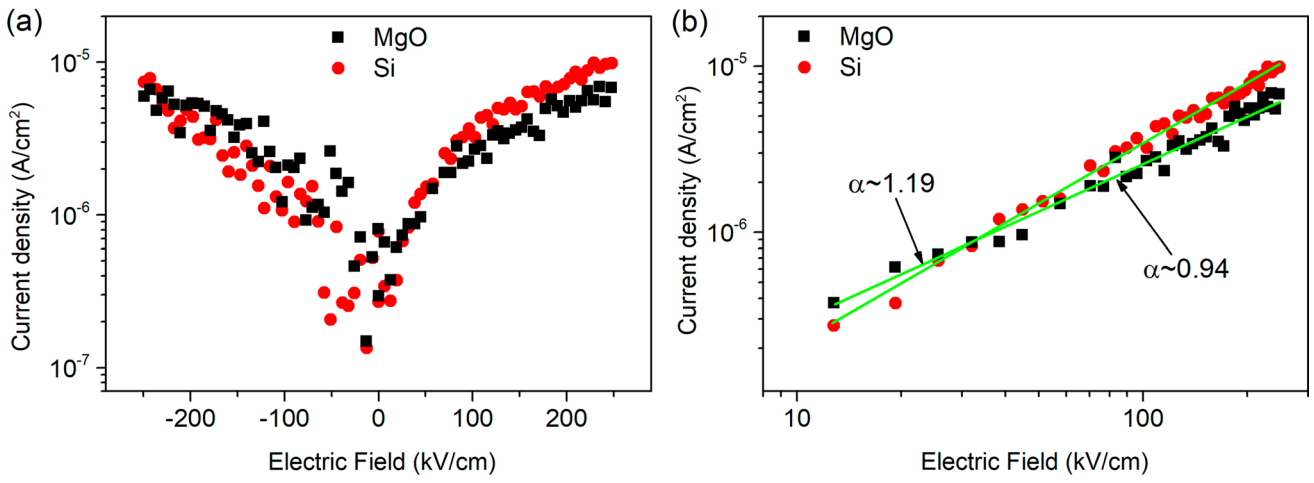

Fig. 5 (a) Leakage current density curve of 9BFZrO thin films on MgO and Si substrates (*J*–*E* curve); (b) leakage current mechanism log(*J*)–log(*E*) curve.

Table 2 Leakage current mechanism

Leakage mechanism	Expression formula	Linear relationship	Conditions met
Ohmic conduction [19]	$J_{Ohmic} = q\mu N_e E$	log(*J*)–log(*E*)	$\alpha \approx 1$
Space charge-limited current (SCLC) conduction [19]	$J_{\mathrm{SCLC}} = \frac{9\mu\varepsilon_r\varepsilon_0}{8d^3}E^2$	log(*J*)–log(*E*)	$\alpha \approx 2$
Schottky emission [37]	$J_{\mathrm{SE}} = AT^2\exp\left(-\frac{\varphi_b}{K_BT}\right)\exp\left(\frac{e\left(\sqrt{\frac{qE}{4\pi\varepsilon_0 K}}\right)}{K_BT}\right)$	$\ln(\mathrm{J/T^2})\&\mathrm{E}^{\frac{1}{2}}$	
Poole–Frenkel (P–F) emission [38]	$J_{\mathrm{PF}} = BE\exp\left[\frac{e\left(\sqrt{\frac{eE}{\pi\varepsilon_0 K}}\right)-E_t}{K_BT}\right]$	$\ln(\mathrm{J/T^2})\&\mathrm{E}^{\frac{1}{2}}$	
Fowler–Nordheim (F–N) tunnelling effect [39]	$J_{\mathrm{FN}} = CE^2\exp\left[-\frac{D^2\sqrt{\varphi_i^3}}{E}\right]$	$\ln(\mathrm{J/E^2})\&\frac{1}{\mathrm{E}}$	

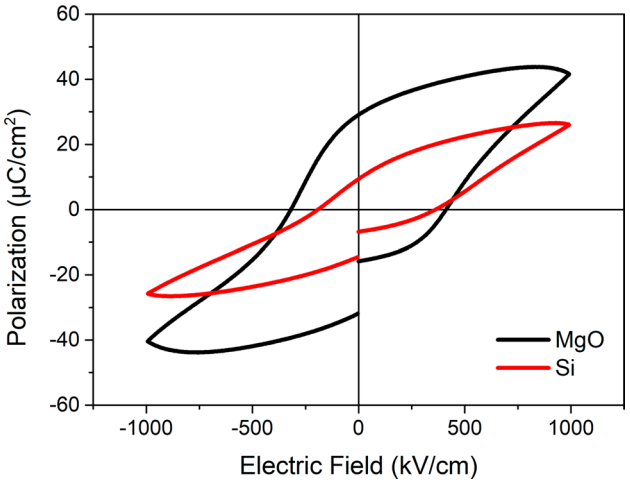

Fig. 6 Hysteresis loop (P–E) diagram of 9BFZrO thin films on MgO and Si substrates

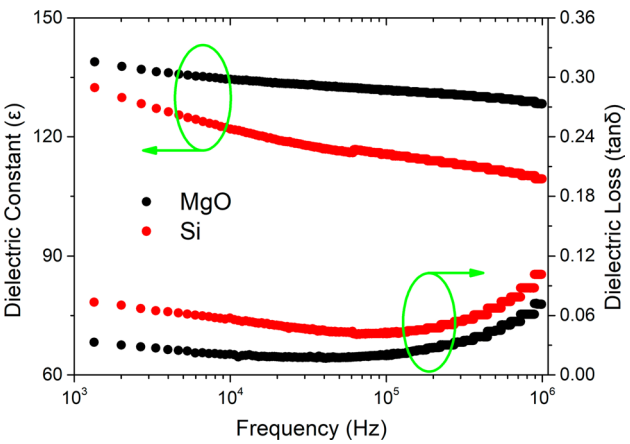

Fig. 7 Frequency-dependent curves of the relative dielectric constant and dielectric loss of 9BFZrO thin films on MgO and Si substrates

substrate exhibited a low degree of ageing and excellent stability. The ageing mechanism of the body involves the formation and rearrangement of defect electric dipoles by the migration of point defects, often oxygen vacancies. In the 9BFZrO thin films, $\left(\mathrm{Fe}^{2+}_{\mathrm{Fe}^{3+}}\right)$ and $(V_{02-})^{\cdot\cdot}$ form ordered defect dipoles $\left[\left(\mathrm{Fe}^{2+}_{\mathrm{Fe}^{3+}}\right)' - \left(V_{O^{2-}}\right)^{\cdot\cdot}\right]$, which align the symmetry of the defects with the crystal and form and internal electric field P_D.[47] After an external electric field E_a is applied, the orientation of the spontaneous polarization P_s is altered; however, the internal electric field P_D remains unchanged.[48] After the external electric field E_a was eliminated, the defect symmetry remained unaltered, and the internal electric field P_D acted as a restorative force, causing the direction of P_s to revert to its initial orientation, as shown in Fig. 8c. According to the XPS analysis above, the sample on the MgO substrate contains a low concentration of defects such as oxygen vacancies and Fe^{2+}, and the pinning effect of the domains is weak. Therefore, the ageing effect caused by the orderly arrangement of defect dipoles, such as $\left[\left(\mathrm{Fe}^{2+}_{\mathrm{Fe}^{3+}}\right)' - \left(V_{O^{2-}}\right)^{\cdot\cdot}\right]$, is weak, and the anti-ageing performance of the film on the MgO substrate is good.

Conclusions

9BFZrO/LNO/MgO and 9BFZrO/LNO/Si multilayers were prepared by the sol–gel method on MgO and Si single crystals as substrates, respectively, and LNO thin films approximately 50 nm thick were used as bottom electrodes and transition layers by magnetron sputtering. The XRD and Raman results indicate that the 9BFZrO thin film samples prepared on MgO and Si substrates have a structure composed of both rhombic *R*3*c* and orthogonal *Pnma* phases. For MgO substrates, the

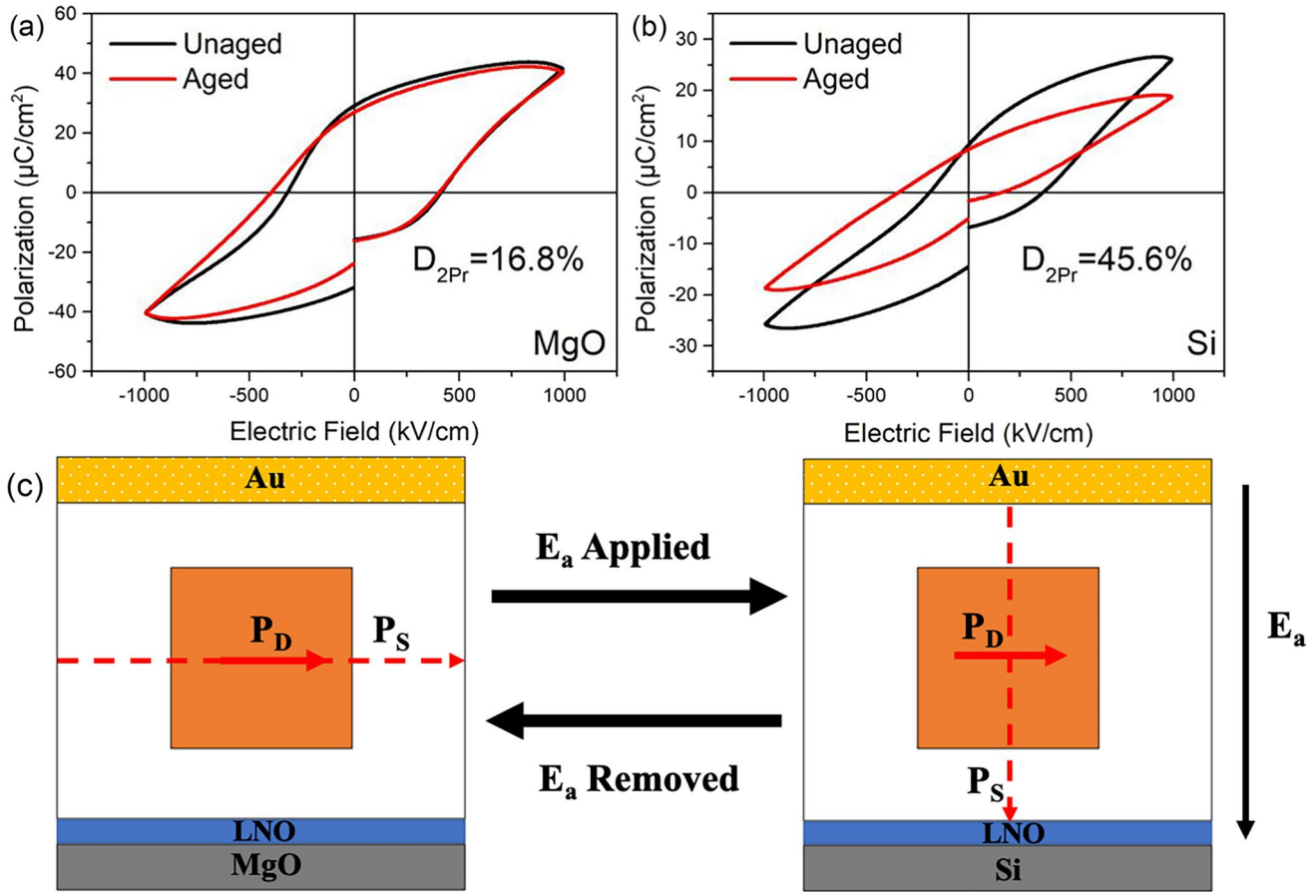

Fig. 8 Comparison of the hysteresis loops of 9BFZrO thin films with MgO and Si substrates at 90-day intervals: (a), (b), and (c) diagram of the ageing mechanism

excessive tensile stress provided by Si substrates results in more orthogonal phases in the samples. SEM analysis revealed that the grains of all the samples were relatively dense, and the thin films prepared on the MgO substrate had relatively large grains. The XPS results indicate that the Fe^{2+} content and oxygen vacancy defect concentration of the thin film prepared on the MgO substrate are relatively low, indicating that excessive lattice mismatch can lead to an increase in Fe^{2+}. At room temperature, a test frequency of 1 kHz, and an electric field intensity of 990 kV/cm, the MgO substrate sample exhibited the maximum residual polarization intensity ($2P_r$=60.28 μC/cm^2). Under a positive electric field of 200 kV/cm, the leakage current density of the thin film on the MgO substrate was approximately 4.71 × 10⁻6 A/cm^2. After 90 days of room-temperature ageing, the residual polarization strength ($2P_r$) of the film on the MgO substrate decreased by 16.8%, with a lower ageing degree and better stability. Therefore, these results indicate that the smaller the substrate lattice mismatch, the more favourable for the formation of structurally stable and electrically sufficient thin films.

Acknowledgments This work was supported by the Shandong Provincial Natural Science Fund (ZR2022ME071).

Conflict of interest The authors declare that they have no known competing financial interests or personal relationships that could have appeared to influence the work reported in this paper.

References

1. V. Sharma, R.K. Ghosh, and B.K. Kuanr, Investigation of room temperature ferromagnetism in transition metal doped $BiFeO_3$. *J. Phys. Condensed Matter.* 31(39), 395802 (2019). https://doi.org/10.1088/1361-648X/ab29d1.
2. Y. Feng, Y. Zhang, J. Sheng, T. Zhang, Q. Chi, Q. Chen, and W. Fei, Multiferroic properties and magnetic anisotropy in P(VDF-TrFE) composites with oriented $CoFe_2O_4$ nanofibers. *J. Phys. Chem. C* 125(16), 8840–8852 (2021). https://doi.org/10.1021/acs.jpcc.0c05792.
3. S. Iqbal, H.M. Rafique, G.M. Mustafa, B. Younas, M. Imran, N. Alwadai, Y. Slimani, and M. Iqbal, Tuning of relaxation phenomenon by substitution of La in $BiFeO_3$. *Mater. Today Commun.* 34, 105337 (2023). https://doi.org/10.1016/j.mtcomm.2023.105337.
4. M. Ait Tamerd, B. Abraime, A. Kadiri, A. Lahmar, M. EL Marssi, M. Hamedoun, A. Benyoussef, and A. El Kenz, Prediction of

magnetoelectric properties of defect $BiFeO_3$ thin films using Monte Carlo simulations. *J. Magnetism Magnetic Mater.* (2021). https://doi.org/10.1021/acs.jpcc.0c05792.
5. J. Li, W. Chen, G. Qian, and J. Cheng, Structure and properties of preferential (110) orientation $BiFeO_3$ thin films by Sol-Gel method. *Integr. Ferroelectr.* 210(1), 161 (2020). https://doi.org/10.1080/10584587.2020.1728856.
6. E.A. Hector, G.M. Chinchay, C.O. Montes-Albino, V. Santos, O.J. Perales, and Perez, Structural and magnetic properties of pure and Mn-doped bismuth ferrite powders. *MRS Advances.* 2(4), 253 (2017). https://doi.org/10.1557/adv.2017.79.
7. A.B. Martinez, N. Godard, N. Aruchamy, M.B. Cosme, O. Condurache, Andreja, S. Glinsek, and T. Granzow, Solution-processed $BiFeO_3$ thin films with low leakage current. *J. Eur. Ceramic Soc.* 41(13), 6449 (2021). https://doi.org/10.1016/j.jeurceramsoc.2021.05.051.
8. S. Gupta, M. Tomar, A.R. James, and V. Gupta, Study of A-site and B-site doping on multiferroic properties of BFO thin films. *Ferroelectrics* 454(1), 41 (2013). https://doi.org/10.1080/00150193.2013.842748.
9. Y. Liu, Z. Ma, Y. Wang, B. Yao, J. He, J. Li, and F. Zhang, Effect of annealing temperature on the properties of $0.5Bi_4Ti_3O_{12}$-$0.5BiFe_{0.98}Mn_{0.02}O_3$ thin films. *Ceram. Int.* 48(19P), 28112 (2022). https://doi.org/10.1016/J.CERAMINT.2022.06.116.
10. S. Gupta, M. Tomar, A.R. James, and V. Gupta, Ce-doped bismuth ferrite thin films with improved electrical and functional properties. *J. Mater. Sci.* 49(15), 5355 (2014). https://doi.org/10.1007/s10853-014-8243-y.
11. F. Yan, M.-O. Lai, and Lu. Li, Enhanced multiferroic properties and valence effect of Ru-doped $BiFeO_3$ thin films. *J. Phys. Chem. C* 114(15), 6994 (2010). https://doi.org/10.1021/jp1009127.
12. A. Huang and S.R. Shannigrahi, Effect of bottom electrode and resistive layer on the dielectric and ferroelectric properties of sol-gel derived $BiFeO_3$ thin films. *J. Alloy. Compd.* 509(5), 2054 (2010). https://doi.org/10.1016/j.jallcom.2010.10.135.
13. K. Wang, X. Shi, R. Gao, J. Wang, Xu. Jiwen, X. Cheng, and H. Huang, Pressure-induced room temperature electrocaloric effect in $BiFeO_3$-$PbTiO_3$ solid solution based on Landau- Devonshire theory. *Mater. Today Commun.* (2022). https://doi.org/10.1016/J.MTCOMM.2022.103396.
14. P. Sutta, Lattice stress gradients in zinc oxide thin films and their influence on the preferentially oriented growth of the films. *Military Acad.* 4413, 27 (2001). https://doi.org/10.1117/12.425445.
15. K. Ujimoto, H. Izumi, T. Yoshimura, A. Ashida, and N. Fujimura, Effect of lattice misfit strain on crystal system and ferroelectric property of $BiFeO_3$ epitaxial thin films. *IOP Conf Series Mater. Sci. Eng.* (2011). https://doi.org/10.1088/1757-899X/18/9/092064.
16. P. Jungmin, G. Fumiya, N. Seiji, K. Takeshi, and O. Masanori, Preparation and characterization of $BiFeO_3$ thin film deposited on ITO substrate by using pulsed laser deposition. *J. Korean Phys. Soc.* 59, 2537 (2011). https://doi.org/10.3938/jkps.59.2537.
17. F.Y. Hou, L.W. Li, D.T. Zhang, W. Wang, W.P. Cao, X.L. Liu, and W.D. Fei, Large piezoelectric response of $BiFeO_3$/$BaTiO_3$ polycrystalline films induced by the low-symmetry phase. *Phys. Chem. Chem. Phys.* 17(17), 11593 (2015). https://doi.org/10.1039/c5cp01320h.
18. S. Wang, H. Wang, J. Jian, J. Chen, and J. Chen, Effects of LNO buffer layers on electrical properties of BFO-PT thin films on stainless steel substrates. *J. Alloy. Compd.* 784, 231 (2019). https://doi.org/10.1016/j.jallcom.2019.01.033.
19. Z. Ma, H. Liu, L. Wang, F. Zhang, L. Zhu, and S. Fan, Phase transition and multiferroic properties of Zr-doped $BiFeO_3$ thin films. *J. Mater. Chem. C.* 8(48), 17307 (2020). https://doi.org/10.1039/D0TC04593D.
20. N. Aruchamy, T. Schenk, V. Kovacova, S. Glinsek, E. Defay, and T. Granzow, Influence of tensile vs. compressive stress on fatigue of lead zirconate titanate thin films. *J. Eur. Ceramic Soc.* 41(14), 6991 (2021). https://doi.org/10.1016/J.JEURCERAMSOC.2021.07.010.
21. H. Klappe and T. Hahn, The application of eigensymmetries of face forms to anomalous scattering and twinning by merohedry in X-ray diffraction. *Acta Crystallograph. Sect. A Found Crystallograp.* 66(Pt3), 327 (2010). https://doi.org/10.1107/S0108767310001091.
22. S. Islam UI Aarif and M. Ikram, Structural stability improvement, Williamson Hall analysis and band-gap tailoring through A-site Sr doping in rare earth based double perovskite La2NiMnO6. *Rare Met.* 38(9), 805 (2019). https://doi.org/10.1007/s12598-019-01207-4.
23. K. Aishwarya and Navamathavan, Effect of grain size and orthorhombic phase of La-doped $BiFeO_3$ on thermoelectric properties. *J. Alloys Comp.* (2023). https://doi.org/10.1016/J.JALLCOM.2023.169452.
24. N.X. Ca, M.Y. Lee, N.T.M. Hong, D.N. Ba, P.T. Tho, N.V. Dang, B.W. Lee, L.T. Ha, L.T. Hue, and C.T.A. Xuan, Peculiar magnetism of $Bi_{1-x}Dy_xFeO_3$ ceramics at the morphotropic phase boundary. *J. Alloy. Compd.* (2021). https://doi.org/10.1016/J.JALLCOM.2021.159331.
25. Y.K. Liu, H.F. Wong, S.Z. Huang, S.X. Hu, S.M. Ng, K.K. Lam, C.L. Mak, and C.W. Leung, Structural, magnetic and transport properties of fully epitaxial LaMnO3/LaAlO3 multilayers. *Mater. Lett.* 205, 230 (2010). https://doi.org/10.1016/j.matlet.2017.06.097.
26. H. Fukumura, S. Matsui, H. Harima, T. Takashashi, T. Itoh, K. Kisoda, M. Tamada, Y. Noguchi, and M. Miyayama, Observation of phonons in multiferroic $BiFeO_3$ single crystals by Raman scattering. *J. Phys. Condensed Matter Inst. Phys. J.* 19(36), 365224 (2007). https://doi.org/10.1088/0953-8984/19/36/365224.
27. A. Monem, N. Abd-Elmohssen, H.H. Ei-Bahnasawy, N. Makram, and K. Sedeek, Comparative studies by X-ray diffraction, Raman, vibrating sample magnetometer and Mössbauer spectroscopy of pure, Sr doped and Sr, Co co-doped $BiFeO_3$ ceramic synthesized via tartaric acid-assisted technique. *Ceramics Int.* 49(10), 15213 (2023). https://doi.org/10.1016/J.CERAMINT.2023.01.103.
28. C. Gumiel, T. Jardiel, D.G. Calatayud, T. Vranken, M.K. Van Bael, A. Hardy, A.C. Caballero, and M. Peiteado, Nanostructure stabilization by low-temperature dopant pinning in multiferroic $BiFeO_3$-based thin films produced by aqueous chemical solution deposition. *J. Mater. Chem. C.* 8(12), 4234 (2020). https://doi.org/10.1039/C9TC05912A.
29. J. Bielecki, P. Svedlindh, D.T. Tibebu, C. Shengzhen, S.G. Eriksson, L. Borjesson, and C.S. Knee, Structural and magnetic properties of isovalently substituted multiferroic $BiFeO_3$: Insights from Raman spectroscopy. *Phys. Rev. B* 86(18), 184422 (2012). https://doi.org/10.1103/PhysRevB.86.184422.
30. M.N. Iliev, M.V. Abrashev, H.G. Lee, V.N. Popov, Y.Y. Sun, C. Thomsen, and R.L. Meng, Raman spectroscopy of orthorhombic perovskite like $YMnO_3$ and $LaMnO_3$. *Phys. Rev. B* 57(5), 2872 (1998).
31. G. Priyanka, A. Ashish, A. Neetu, and S. Suiata, Crystal structure, dielectric and magnetic properties of Gd doped $BiFeO_3$ multiferroics. *Phys. B Phys. Cond. Matter.* 550, 414 (2018). https://doi.org/10.1016/j.physb.2018.08.045.
32. S. Ayan, Singh Ashutosh K and Sarkar Debasish, Three-dimensional nanoarchitecture of $BiFeO_3$ anchored TiO_2 nanotube arrays for electrochemical energy storage and solar energy conversion. *ACS Sust. Chem. Eng.* 3(9), 2254 (2015).
33. S.K. Singh, C.V. Tomy, T. Era, M. Itoh, and H. Ishiwara, Improved multiferroic properties in Sm-doped $BiFeO_3$ thin films deposited using chemical solution deposition method. *J. Appl. Phys.* 111(10), 102801 (2012). https://doi.org/10.1063/1.4714650.

34. C. Raghavan, M. Hinnambedu, J.W. Kim, and S.S. Kim, Effects of Ho and Ti doping on structural and electrical properties of $BiFeO_3$ thin films. *J. Am. Ceramic Soc.* 97(1), 235 (2014). https://doi.org/10.1111/jace.12641.
35. E. Cao, Y. Qin, T. Cui, Li. Sun, W. Hao, and Y. Zhang, Influence of Na doping on the magnetic properties of $LaFeO_3$ powders and dielectric properties of $LaFeO_3$ ceramics prepared by citric sol-gel method. *Ceram. Int.* 43(10), 7922 (2017). https://doi.org/10.1016/j.ceramint.2017.03.119.
36. Yu. Zhiqiang, Qu. Xiaopeng, W. Yang, J. Peng, and Xu. Zhimou, Hydrothermal synthesis and memristive switching behaviors of single-crystalline anatase TiO_2 nanowire arrays. *J. Alloy. Compd.* 688, 294 (2016). https://doi.org/10.1016/j.jallcom.2016.07.216.
37. W. Jiagang, W. John, X. Dingquan, and Z. Jianguo, Leakage mechanism of cation-modified $BiFeO_3$ thin film. *AIP Adv.* (2011). https://doi.org/10.1063/1.3601362.
38. P.M. Raj, B.W. Lee, D. Balaraman, and R.R. Tummala, Leakage current analysis of hydrothermal $BaTiO_3$ thin films. *J. Electroceramics.* 27(3–4), 169 (2011). https://doi.org/10.1007/s10832-011-9662-7.
39. Y. Feng, Z. Fuwei, H. Guangda, Z. Zhihao, and T. Minghua, Thickness-dependent ferroelectric behavior of predominantly (117)-oriented $Bi_{3.15}Nd_{0.85}Ti_3O_{12}$ thin-film capacitors. *Appl. Phys. Lett.* (2015). https://doi.org/10.1063/1.4919566.
40. H.M. Christen, J.H. Nam, H.S. Kim, A.J. Hatt, and N.A. Spaldin, Stress-induced R-MA-MC-T symmetry changes in $BiFeO_3$ films. *Phys. Rev. B* 83(14), 144107 (2011). https://doi.org/10.1103/PhysRevB.83.144107.
41. Z. Chen, Lu. Yajun Qi, P.Y. You, J. Wang, S. Thjrumang, and L. Chen, Large tensile-strain-induced monoclinic MB phase in $BiFeO_3$ epitaxial thin films on a $PrScO_3$ substrate. *Phys. Rev. B* 88(5), 054114 (2013). https://doi.org/10.1103/PhysRevB.88.054114.
42. C. Huang and L. Chen, Effects of interfaces on the structure and novel physical properties in epitaxial multiferroic $BiFeO_3$ ultrathin films. *Materials.* 7(7), 5403 (2014). https://doi.org/10.3390/ma7075403.
43. G. Rongli, Z. Qingmei, X. Zhiyi, W. Zhenhua, C. Gang, D. Xiaoling, F. Chunlin, and C. Wei, A comparative study on the structural, dielectric and multiferroic propertiesof $Co_{0.6}Cu_{0.3}Zn_{0.1}Fe_2O_4/Ba_{0.9}Sr_{0.1}Zr_{0.1}Ti_{0.9}O_3$ composite ceramics. *Comp. Part B.* 166, 204 (2019). https://doi.org/10.1016/j.compositesb.2018.12.010.
44. G. Rongli, Q. Xiaofeng, Z. Qingmei, X. Zhiyi, W. Zhenhua, F. Chunlin, C. Gang, D. Xiaoling, and C. Wei, Enhancement of magnetoelectric properties (1-x)$Mn_{0.5}Zn_{0.5}Fe_2O_4$-x $Ba_{0.85}Sr_{0.15}Ti_{0.9}Hf_{0.1}O_3$ composite ceramics. *J. Alloys Comp.* 795, 501 (2019). https://doi.org/10.1016/j.jallcom.2019.05.013.
45. R. Gao, Z. Wang, G. Chen, X. Deng, W. Cai, and Fu. Chunlin, Inuence of core size on the multiferroic properties of $CoFe_2O_4$@ $BaTiO_3$ core shell structured composites. *Ceram. Int.* 44, S84 (2018). https://doi.org/10.1016/j.ceramint.2018.08.234.
46. C.H. Yang, S.D. Wang, and D.M. Yang, Fabrication and properties of silicon-based $(Bi, Sm)_4Ti_3O_{12}$ thin film. *J. Alloy. Compd.* 467(1), 434 (2009). https://doi.org/10.1016/j.jallcom.2007.12.059.
47. X. Ren, Large electric-field-induced strain in ferroelectric crystals by point-defect-mediated reversible domain switching. *Nat. Mater.* 3(2), 91 (2004).
48. C.M. Folkman, S.H. Baek, C.T. Nelson, H.W. Jang, T. Tyball, X.Q. Pan, and C.B. Eom, Study of defect-dipoles in an epitaxial ferroelectric thin film. *Appl. Phys. Lett.* 96(5), 052903 (2010). https://doi.org/10.1063/1.3298362.